Geophysical Journal International

Geophys. J. Int. (2012) **188,** 737–749 doi: 10.1111/j.1365-246X.2011.05267.x

Crustal structure and deformation in the northeast India–Asia collision zone: constraints from receiver function analysis

Devajit Hazarika[1], B.R. Arora[2] and Chandan Bora[1]

[1] *Wadia Institute of Himalayan Geology, Dehradun* 248 001, *India. E-mail: devajit_h@rediffmail.com*
[2] *Uttarakhand Council for Science & Technology,* 6, *Vasant Vihar Phase I, Dehradun* 248 006, *India*

Accepted 2011 October 13. Received 2011 October 13; in original form 2010 December 26

SUMMARY

Crustal structure across the India–Asia collision zone (Tidding Suture) in the northeast Himalaya bounded by the Eastern Himalayan Syntaxis (EHS) is investigated using the *P*-wave receiver function (RF) method. The analysed data included three-component waveforms of teleseismic earthquakes recorded by a linear array of 11 broad-band seismic stations. The RFs and inverted shear wave velocity models reveal azimuthally varying crustal structure. The RFs for earthquakes from the northeast back azimuths are conspicuous by absence of *P*-to-*S* converted phase at the Moho discontinuity. Inverted velocity model ascribe this to absence of the typical step velocity jump at the Moho in a narrow section of the EHS bordering the indenting Indian Plate and pierced by travelling waves. In contrast, teleseismic waves arriving from southeast back azimuth sample different litho-tectonic blocks of the Himalayan collision zone and inverted models show northeast dipping Moho across the Tidding Suture. Compared to an overall thickness of >70 km in the northwest and central Himalaya, the crust across the Tidding Suture is only about 55 km thick. This is attributed to a slower rate of convergence in this part of the collision zone. The Moho structure beneath Indian Plate and southeastern Tibetan Plateau reveal opposite dip directions with their colliding margin placed just east of the Walong Thrust. The inverted shear wave velocity models show evidence of intracrustal low-velocity layer whose strength varies across the Tidding Suture. The magnitude of velocity reduction beneath Lohit Plutonic Complex (Trans Himalaya) favour partial melt as a possible mechanism whereas south of the Tidding Suture, where velocity reduction is comparatively less, fluids generated by dehydration reactions appear to be the source for velocity reduction.

Key words: Plate motions; Magnetotelluric; Broadband seismometers; Subduction zone processes; Crustal structure; Rheology: crust and lithosphere.

1 INTRODUCTION

The building of lofty Himalaya and elevated Tibetan Plateau are the manifestation of ongoing collision between Indian and Asian plates over the last 45 Ma (Bird 1978; Mattayer 1986; Molnar 1988). Much of the continent-collision convergence along the east–west extending Himalayan arc is consumed by crustal shortening of more than 1500 km (Molnar & Tapponnier 1975). Several competing mechanisms proposed to attain crustal shortening include crustal thickening (LeFort 1975; Allegre *et al.* 1984), underthrusting of Indian mantle lithosphere (Ni & Barazangi 1984; Tilmann *et al.* 2003; Kumar *et al.* 2006; Rai *et al.* 2006; Li *et al.* 2008), lithosphere detachment (Kosarev *et al.* 1999), underplating (Nabelek *et al.* 2009), subduction of the Asian lithosphere (Kind *et al.* 2002), channel flow (Beaumont *et al.* 2001) and escape tectonics (Tapponnier *et al.* 1982; Replumaz & Tapponier 2003). Early analogue modelling indicated dominance of escape tectonics between southeast Tibet and the Eastern Himalayan Syntaxis (EHS) by the way of eastward extrusion of Indo-China block along the Red River fault (Tapponnier *et al.* 1982, 1990). The GPS velocity vectors coupled with images of lithospheric structure demonstrated that eastward crustal escape flow in the southeastern part of the Tibetan Plateau is deflected by the resistive Sichuan Basin to produce deformation pattern consistent with rotation of crustal blocks around the EHS (Zhang *et al.* 2009, 2010; Xu *et al.* 2007). The mapped crustal variations across the Longmen Shan (LMF) fault separating the Southeast Tibetan Plateau from the rigid Sichuan Basin provide conditions to support lower crustal channel flow. More recently, resistivity imaging by magnetotelluric measurements have mapped two high electrical conductivity zones at crustal depths of 20–40 km (Bai *et al.* 2010). The high electrical properties of the material embedded in this zones warrant an elevated fluid content implying weak crust. These evidences were used by Bai *et al.* (2010) to suggest intense crustal flow along two arcuate channels, paralleling the geometry of the EHS, from the southeastern Tibet Plateau to southwest China (Fig. 1a).

Although the role of indenting Indian Plate on the evolution and dynamics of the EHS is clearly emerging, the deep lithospheric

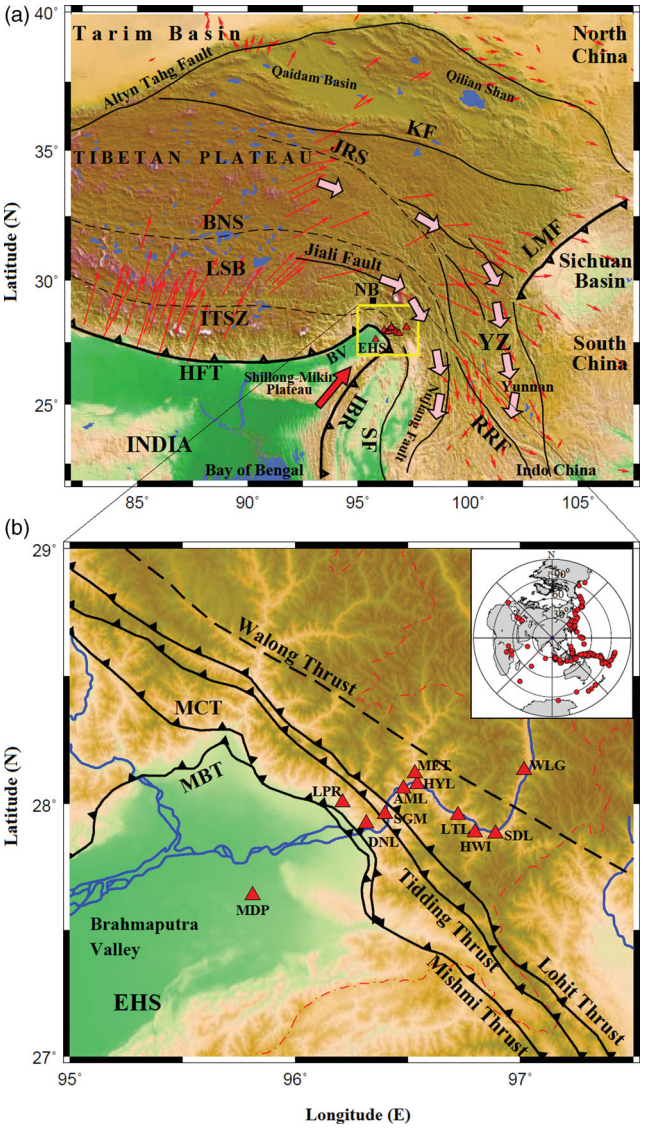

Figure 1. (a) Topographic map of the Eastern Himalayan Syntaxis and surrounding regions with major tectonic features: (1) Himalayan Frontal Thrust (HFT), (2) Indo-Burma Ranges (IBR), (3) Indus-Tsangpo Suture Zone (ITSZ), (4) Lhasa Block (LSB), (5) Bangong Suture (BNS), (6) Jinsha River Suture (JRS), (7) Longmen Shan Fault (LMF), (8) Sagaing Fault (SF), (9) Kunlun Fault (KF), (10) Namche Barwa Antiform (NB), (11) Yangtze platform (YZ), (12) Brahmaputra Valley (BV) (modified after Gururajan & Choudhary 2003; Tapponnier *et al.* 2001). The boxed area marks the study area. Red thin arrows denote GPS-derived surface velocities relative to the stable Asia (Wang *et al.* 2001) and red thick arrow indicates surface velocities in NE India (Jade *et al.* 2007). The thick pink arrows trace the path of crustal flow channels in SE Tibetan plateau (Bai *et al.* 2010). (b) Close view of the study area with locations of 11 broad-band seismological stations along the Lohit River Valley against the back drop of major tectonic features of the colliding India-Asia Plate. The inset shows distribution of teleseismic earthquakes (red filled circles) used for *P*-wave receiver function analysis.

structures and deformation of the Indian Plate in the indenting northeast corner have largely remained unexplored. This paper provides new information on crustal structure and Moho discontinuity along a linear profile extending from the Brahamaputra Valley to Lohit Plutonic complex, Arunachal Pradesh (Fig. 1a) by applying the *P*-wave receiver function (RF) technique (Vinnik 1977; Langston 1979). The selected linear profile is significant as it cuts across the mega thrust zones and suture related with evolution of the Himalaya. An added feature of the layout of the present profile is that it fills vital spatial gaps covered by previous passive seismological studies in northeast India in the west (Kumar *et al.* 2004; Mitra *et al.* 2005) and the Yangtze platform and Sichuan Basin of the southeastern Tibet Plateau in the east (Xu *et al.* 2007; Zhang *et al.* 2009, 2010). The data from the present and previous studies are integrated to discuss results in context to the regional tectonics. The earlier study of Singh (1994) established the shear wave velocity structure of the eastern India on regional scale. It served as a useful guide in providing the initial model for velocity inversion carried out in this study.

2 GEOLOGY AND TECTONICS OF THE STUDY AREA

Flanking the Indian Plate on the northeast corner, the ENE–WSW trending Himalayan collision zone takes a sharp bend to wrap around NW–SE trending Mishmi Hills (Fig. 1a). This sharp bend enclosing the Namche Barwa antiform is referred to as the Eastern Himalayan Syntaxis (EHS). In the plate tectonic model, the EHS is viewed as a complex triple junction that joins the Indian and Asian plates with northern end of the Burma platelet. The EHS marks a fundamental tectonic change, transitioning from collision dominated tectonics along the E–W trending Himalaya to strike slip tectonics in the southeast Tibet/Sagaing Fault (Holt *et al.* 1991). On the regional scale, the most significant tectonic unit to the north and northeast of the EHS is the southeastern Tibetan Plateau separated from the stable Sichuan basin by highest topography marked by Longmen Shan (LMF) fault (Zhang *et al.* 2010). Immediately east of the EHS is the Yangtze Platform (YZ), Yunnan Province, bounded on the southwest by the Red River Fault (RRF) of south China (Fig. 1). Further southeastward, the EHS provides a link to the N–S oriented strike slip Sagaing fault (SF) merging further south with the N–S trending Indo-Burmese arc. The most dominant structural unit in the west of the EHS is the Shillong Plateau of Northeast India.

The linear profile selected for this passive seismology experiment is located along the Lohit River valley section on eastern limb of the EHS (Fig. 1b). The geology and tectonics of the study area overlapping with the geographic area of eastern Arunachal Pradesh has been described by Gansser (1964), Thakur & Jain (1975) and Gururajan & Choudhary (2003) among several others. On the Lohit Valley section, the Outer-Himalayan Siwalik sequence, a prominent feature of the Himalayan Arc, is conspicuously absent. Instead, a narrow pinched out Lesser Himalayan sequence rests on a thick pile of alluvium in the Brahamaputra Valley (outer Himalaya foredeep) along the Mishmi Thrust (Main Boundary Thrust, MBT). The Main Central Thrust (MCT) separates the Lesser Himalaya from the Mishmi Crystalline, equivalent of the High Himalayan Crystalline. The Tidding Suture Zone overriding the Mishmi crystalline on the southwest and bounded by the Lohit thrust on the northeast contains rich preserves of ophiolitic melange and is interpreted as southeast continuation of the Indus-Tsangpo Suture Zone (ITSZ) exposed all along the Himalayan arc. The Lohit Plutonic Complex, equivalent of Trans Himalayan Ladakh and Gandesse Batholiths in the northwest and central Himalaya respectively, is further subdivided into western and eastern belts separated by the Walong thrust (Gururajan & Choudhary 2003). The presence of intrusive rocks in the eastern

belt are considered marker of magmatism related to the subduction, far away from the Indo-Burmese subduction zone.

The profile selected for deployment of seismographs for passive seismic experiments runs at right angles to strike of the major tectonic features to the extent permitted by rugged topography and accessible roads. The 11 stations established across the Tidding Suture extend from the Brahamaputra Valley to the Lohit Plutonic complex, east of the Walong thrust. The seismograph at Mahadevpur (MDP) is located on the thick sediments of the Brahmaputra valley; Luhitpur (LPR) and Dasnala (DNL) lie on the Mishmi crystallines east of the Mishmi thrust; Salangam (SGM) is located on the Metavolcanic rocks of Tidding Suture Zone. The seismograph stations at Amliang (AML), Metalliang (MET), Hiyuliang (HYL), Latul (LTL), Hawai (HWI) and Samdul (SDL) are located on western belt of the Lohit Plutonic Complex. The seismograph station at Walong (WLG) is located on eastern belt of the Lohit Plutonic Complex.

3 DATA

The data used in this study have been recorded on 11 three-component broad-band seismometers located in Brahmaputra and Lohit River Valleys (Fig. 1b). Each station was equipped with Trillium 240 seismometers with a flat velocity response between 0.004 and 35 Hz and streams of data with 20 samples s^{-1} were recorded on Taurus data logger with 56 dB gain (Make M/S Nanometrics, Canada). The GPS receivers are used for time synchronization. These stations were operated during the period April 2007 to August 2008. The records of teleseismic earthquakes were used to study the crust and upper-mantle structure along the study profile using the RF approach (Langston 1979*)*. During this period, waveform data of total 150 teleseismic earthquakes meeting the following criteria were selected: (1) body-wave magnitude $m_b >$ 5.5 to favour high signal-to-noise ratio, (2) epicentral distances (Δ) between 30° and 90° to avoid wavefield complexities due to upper-mantle discontinuities (Xu *et al.* 2007). Information for teleseismic earthquakes is extracted from PDE catalogue of US Geological Survey (http://neic.usgs.gov). The geographical distribution of epicentres of the earthquakes selected for the study is shown in Fig. 1(b) (inset). The earthquakes are mostly from the Circum-Pacific seismogenic belt. The azimuthal distribution of earthquakes is similar to those reported in other experiments from this region conducted in different periods (Xu *et al.* 2007; Zhang *et al.* 2010).

4 METHODOLOGY AND RESULTS

4.1 Receiver function analysis

The RF method is a well-established seismological technique to determine crust and upper-mantle velocity structure beneath three-component broad-band seismograph site (Vinnik 1977; Langston 1979; Kind *et al.* 1995). As a teleseismic *P*-wave propagates through the upper mantle and crust towards a seismic station, intervening discontinuities cause a fraction of the *P*-wave energy to be converted to *S*-waves. These *P*-to-*S* converted phases and their reverberations recorded on the two horizontal components can be isolated from the source time function and propagation effects by deconvolving the vertical component of the seismogram from the radial and transverse components to get radial and transverse component RF, respectively. The radial RF closely corresponds to the impulse response of the earth structure beneath a seismic receiver, whereas the transverse component RF, which is expected to be zero for an ideal homogeneous, isotropic, horizontally stratified crust, accordingly provides a measure of deviation of the underlying crustal structure from these ideal conditions. The inversion of amplitude and timing of converted phases and their reverberations provide constraints on the underlying crustal structure. Computation of RFs requires several processing steps; including pre-processing of the raw data, rotation into the ray coordinate system, deconvolution and stacking (Vinnik 1977). Pre-processing of the raw data consisted of re-sampling the data to 10 samples/s by applying a Gaussian low-pass filter corresponding to a 1.5 s pulse width, cutting the data to include no more than 60 s before and 100 s after the *P*-wave arrival, and finally tapering the ends of the cut seismograms. We have computed about 950 individual RFs for 11 broad-band seismological stations using the iterative, time domain deconvolution technique of Ligorria & Ammon (1999). This technique constructs RF by minimizing the difference between the observed radial seismogram and the convolution of the iteratively updated Gaussian-sum time series (RFs) with the observed vertical seismogram.

To illustrate the details of the adopted methodology, the analysis of data for station AML is discussed here. Fig. 2(a) shows moveout corrected 39 radial RFs for the station AML plotted as a function of back azimuth (BAZ) ranging between 38° and 300°. The RFs for the earthquakes from NE back azimuths (BAZ: ∼30°–80°) are referred hereafter as NE group, whereas RFs outside this band of BAZs are collectively referred to as SE group. In addition, the selected RFs, both radial and tangential, for a narrow bin of back azimuths (BAZ = 110°–121°) are plotted in Fig. 3 for range of epicentral distances (31°–90°). The most immediate feature of Fig. 2(a) is that individual RFs show strong dependence on the BAZs. In the BAZ range of 105°–174°, the most clear and strong positive arrival is seen at 6.5 ± 0.5 s. Further, delay time of this positive arrival with increasing range of epicentral distances tends to align on to a single plane placed parallel to direct *P*-arrival (Fig. 3). This coupled with delay time of about 6.5 s favours to attribute this phase to the Moho converted *P*-to-*S* (P_ms) phase. Therefore, individual RFs in Figs 2(a) and 3 are plotted after distance moveout correction for the P_ms phase to a reference distance of 67° and slowness 6.4 s deg^{-1}. In contrast to this band of BAZ, majority of the individual RFs for the earthquakes from NE group do not show clear positive arrival around 6.5 s. Because the amplitude of the RFs is determined by velocity contrast at the discontinuity, we show later that the absence of phase P_ms for the NE marks gradational velocity jump at the Moho.

In addition to the azimuth-dependent P_ms phase, the individual radial RFs show range of arrivals before and beyond the coherent phase at 6.5 s (Figs 2a and 3) but individual arrivals, particularly late ones, present a scattered picture making characterization of converted and their multiples ambiguous and difficult. Identification of converted phases and their multiples in the observed RFs is facilitated with the help of ray paths and synthetic RF corresponding to a representative velocity model (Fig. 4). A technique based on propagator matrix (Kennet 1983) is used to compute the synthetic RFs for a given velocity model. The main purpose of this simulation exercise was to have *a priori* knowledge of the nature and expected time delays of various converted phases and their multiples. The exercise simulates observations as closely as possible the selection of velocity model was guided by the velocity structure obtained by inversion of the observed RFs, discussed in the later sections. The selected model included Moho discontinuity and an intracrustal low-velocity layer (IC-LVL). This exercise to establish origin of the specific phases was further supplemented by computing numbers

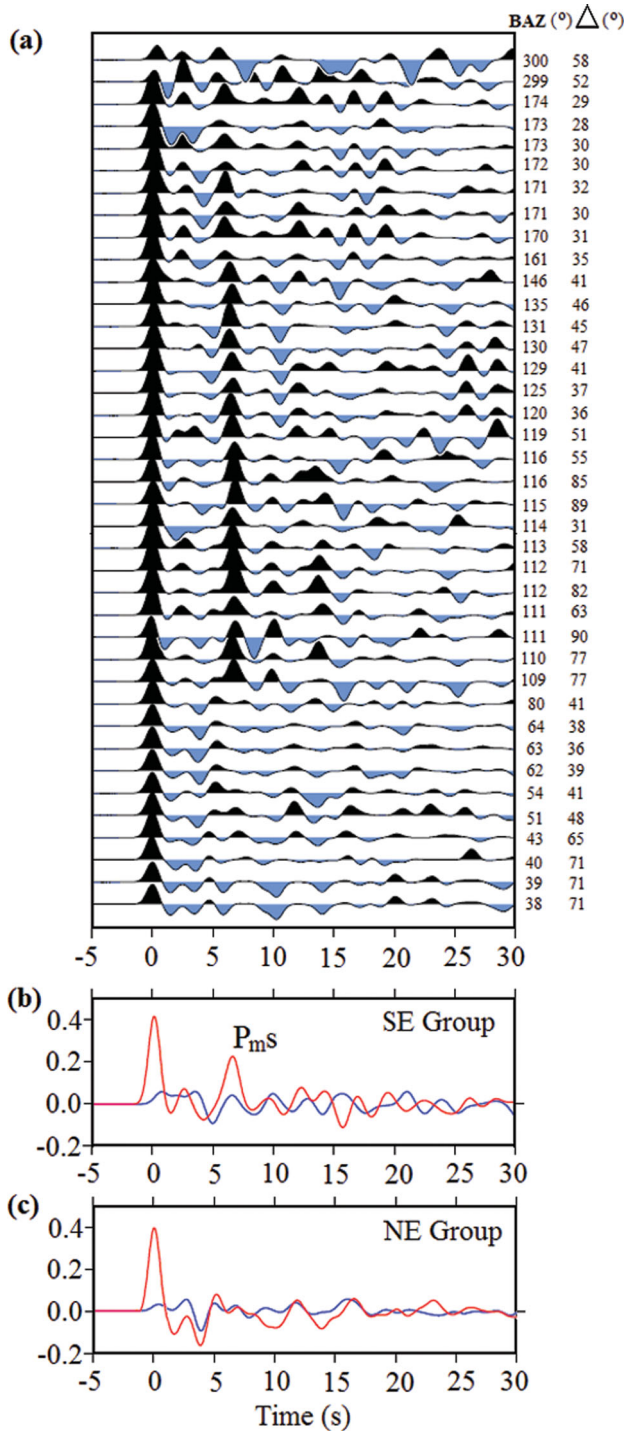

Figure 2. Plots of (a) individual radial receiver functions as a function of back azimuth for AML seismic station. The earthquakes arriving from northeast direction (BAZ: ∼30°–80°) do not show clear P_ms phase whereas it is clearly identified at about 6.5 s for earthquakes from other directions (SE group) after the direct P wave (0.0 s). The stacked radial (red) and tangential (blue) RFs for (b) SE and (c) NE group of earthquakes are shown separately. The traces are moveout corrected for P_ms phase to a reference distance of 67° and slowness 6.4 s deg^{-1}.

of synthetic radial RFs, each time considering only one prominent velocity feature (Fig. 5). In the velocity model when Moho with sharp velocity jump only is considered (model a in Fig. 5), dominant features of the synthetic RF are a strong positive phase around 6 s and positive-negative multiples, respectively, around 22 and 27 s (Fig. 5a) designated respectively as P_ms, PpP_ms, PpS_ms phases in Fig. 4. In this representative model, when an IC-LVL is introduced (model c in Fig. 5), a series of negative-positive-negative phases appear before the Moho phase and positive–negative couplet is seen around 12 and 16 s (Fig. 5c). Before the most dominant P_ms phase, the prominent phases in synthesized RF are the presence of negative arrivals centred at ∼1.5 and ∼3.5 s with embedded positive arrival around 2.5 s (Figs 4 and 5c). It follows from ray paths (Fig. 4) and synthesized RFs in Figs 4 and 5c that the negative and positive phases at 1.5 and 2.5 s can, respectively, be related to converted phases from the top (P_ts) and bottom (P_bs) interfaces of the IC-LVL whereas negative phase at 3.5 s defines free multiple reflection of the converted P_ts phase from the surface (PpP_ts). The combination of converted and multiples with some degree of variability can be traced in individual plots of observed RFs in Figs 2 and 3. In the moveout corrected plots in Fig. 3, the phases around 3.5 and 15 s show an increasing time delay with increasing epicentral distance, consistent with their multiple origin. As multiples from different crustal interfaces travel longer distances in the crust compared to the direct converted phases, they are more prone to scattering and velocity heterogeneity. Secondly, the moveout correction for the direct conversion introduces variable time delay in the arrival of multiples and hence they do not line up parallel to the direct conversation, like P_ms phase. A possible consequence of the above two factors is that Moho associated multiples in the period band of 20–27 s do not align coherently in the observed RFs of the station AML (Figs 2 and 3). However, the coherent late multiples appear in the RF plots of select stations in Fig. 6(b).

The lower panels in Fig. 2 give the stacked plots of RFs, separately for SE and NE groups (Figs 2b and c). In comparison to the amplitudes of radial RFs, the tangential components are small but not negligible. The presence of weak but coherent tangential component would signify dipping interfaces, scattering, anisotropy, and/or azimuth-dependent laterally heterogeneous structure (Cassidy 1992; Savage 1999). Low value of energy at zero time (Fig. 2c) is a pointer of the lack of steep dipping layer (Savage 1998). The use of only teleseismic earthquakes in the computation of RFs ensures that seismograms are free from the far-field scattered energy (Nolet and Dahlen 2000). The azimuth-sensitive radial RFs are clear pointer of laterally heterogeneous structure, weak but coherent tangential RFs near P_ms do not rule out presence of weak crustal anisotropy.

4.2 Receiver functions at all sites of the transect

The three-component waveform data of teleseismic earthquakes recorded at 11 stations along this study profile were analysed using RF method described earlier. A common feature of the computed RFs at all stations is that, the converted P_ms phase, both in amplitude and sharpness, varies for earthquakes arriving from different azimuths. The majority of RFs at different stations computed for the teleseismic waves arriving from BAZ∼30°–80° do not show clear P_ms phase (Fig. 6a). In contrast, RFs for the earthquakes entering the region from other directions show strong P_ms phase (Fig. 6b). Because the variations in the RFs with back azimuths are pointer of the lateral variation of crustal structure (Xu *et al.* 2007), to bring out the azimuth-dependent crust–mantle structure in the indenting Indian Plate, the stacked radial RFs of different stations are processed separately for NE and SE groups (Figs 6a and b). The absence of Moho phase in the RFs for the NE group, noted earlier in the RFs of

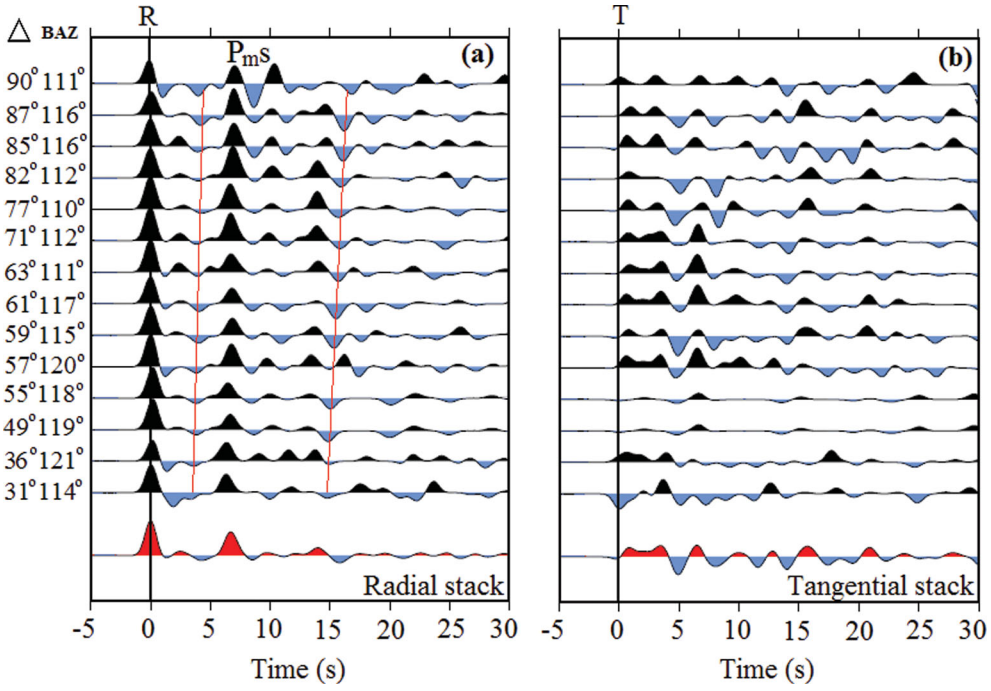

Figure 3. (a) Radial and (b) tangential receiver functions (moveout corrected for P_ms phase) of AML station for specific back azimuth (BAZ = 110°–121°) plotted as function of epicentral distances (Δ) within the range 31°–90°. The red lines at ∼3.5 and ∼15 s show expected moveout of surface multiples of converted phases from the top and bottom of the IC-LVL. Stacked RFs are shown as red waveforms at the bottom.

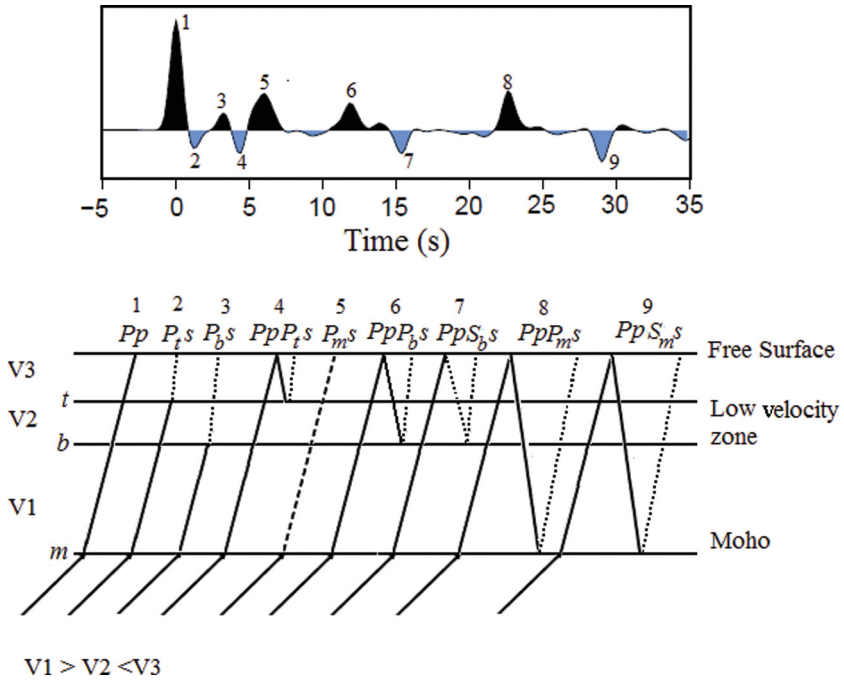

Figure 4. Figure showing a synthetic RF and corresponding ray paths of *P*-to-*S* converted phases for a three layer media with velocity V1, V2 and V3, respectively, from bottom to top surface where V1>V2<V3. The layer with velocity V2 represents intracrustal low-velocity layer (IC-LVL) as shown in Fig. 5c. The Moho as well as the top and bottom surface of the IC-LVL is marked as m, t and b, respectively. The selective converted phases from these interfaces are accordingly indicated by suffices m, b and t, respectively. The solid line indicates *P*-wave ray path and the dashed line indicates *S*-wave ray path.

station AML, is a conspicuous feature of all stations. The dominant feature of the RFs for the SE group is the P_ms phase, whose delay time with respect to the direct *P* arrival increase from 5.9 s beneath the Brahmaputra valley (MDP station) to ∼7.8 s east of Tidding Suture Zone and Lohit thrust (MET and HYL stations), indicating a progressive deepening of Moho towards northeast. The decreasing trend of delay time (∼6 s) at stations LTL, HWI and SDL suggest marginal rise in the depth of Moho. The RFs of MDP station located

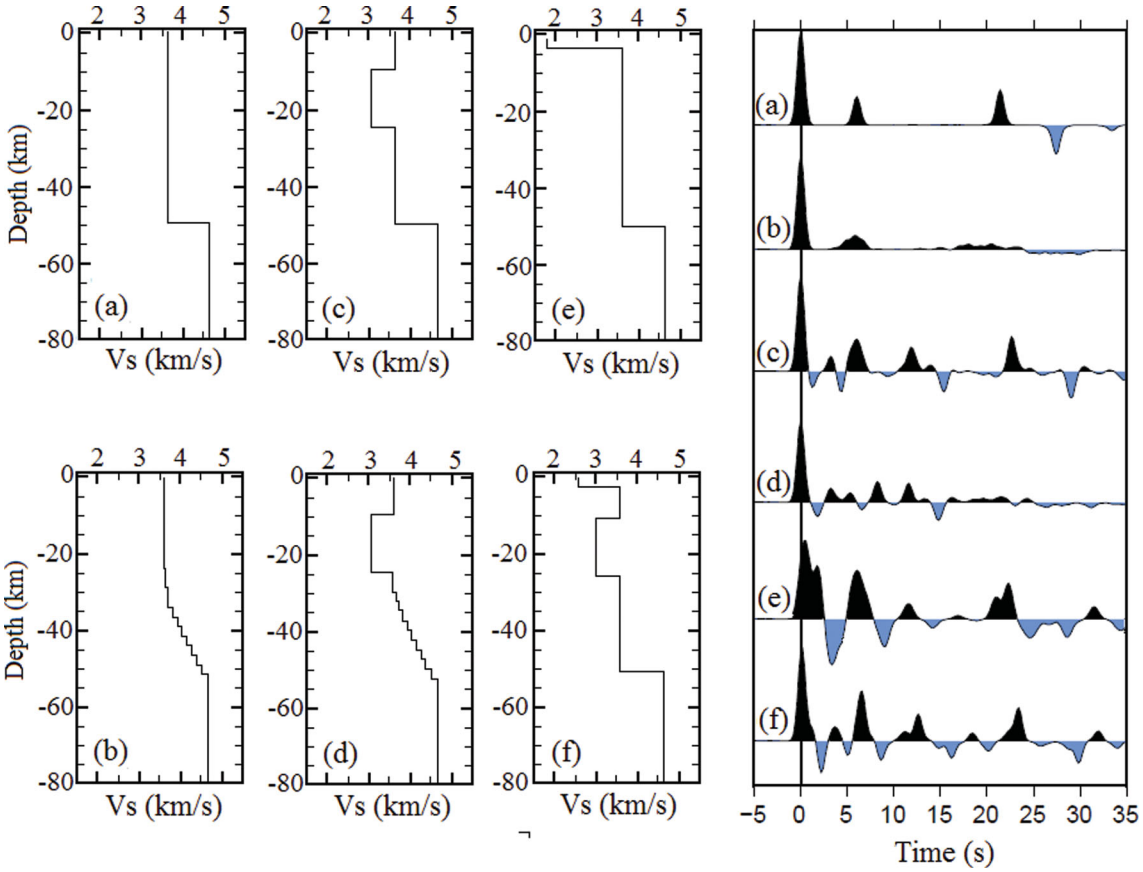

Figure 5. Results of numerical experiment on effect of several prominent features present in a given velocity model on the corresponding synthetic seismogram. The elementary test-velocity models incorporating the sharp (a) and gradational (b) velocity transition at Moho as noted in the representative velocity models for the SE and NE groups are constructed. The above base models are upgraded by first introduction of IC-LVL (c and d) and subsequently by adding S-LVL with and without IC-LVL (e and f). The effect of different interfaces on the computed synthetic RFs is shown in the extreme right panel.

in the sediment filled Brahmaputra valley show a delay of ∼1 s in arrival of the *P* wave, as a consequence, the peak of first arrival (*Pp* phase) is broadened. The delay in first *P* wave can be attributed to the presence of thick pile of low-velocity sediments beneath the station (van der Meijde *et al.* 2003; Xu *et al.* 2007). This inference is corroborated by the synthetic RFs for a velocity model where surface low-velocity layer (S-LVL) and Moho are considered dominant features of the velocity structure with or without IC-LVL (models e and f in Fig. 5). Consistent with observed signature at station MDP, superposition of a positive arrival at ∼1 s broadens the peak of first arrival (*Pp* phase).

Further, consistent with the synthetic tests, the subsequent pairs of positive and negative arrivals, corresponding to delay time of ∼12–14 and ∼16 s, with varying amplitude and sharpness can be traced in the RFs of most of the stations both for the NE and SE groups (Fig. 6a and b). In respect of the late positive arrivals around 20–22 s and negative arrival centered on 25–27 s, two significant observations are: (i) for the NE group where primary converted P_ms phase itself is not observed, the expected late arrivals are conspicuously absent (Fig. 6a) and (ii) although no where well marked in the individual RFs of station AML (Fig. 3), these late arrivals appear well above the back ground noise level at number of stations for the SE group (Fig. 6b). Because individual RFs in Figs 6(a) and (b) are organized with increasing epicentral distances, the alignment of these late arrivals on a dipping plane in relation to direct arrival of *Pp* phase for the SE group coupled with their absence for the NE group are consistent with their origin as multiple. Judging by their polarity and relative arrival times, the first pair of late arrivals can be interpreted, respectively, as multiples reflection of the intracrustal phases and Moho converted phases from surface, indicated as ($PpP_bs + PpS_bs$) and ($PpP_ms + PpS_ms$) phases in Fig. 4). The RF of WLG shows three positive phases with equal energy at around 5.5, 9.5 and 12 s respectively, indicating local complexity of structure associated with the Walong thrust.

4.3 Crustal structure modelling

Given the sensitivity of radial RF to subsurface *S*-wave velocity, velocity structure beneath recording sites is determined by inverting the radial RF waveforms using the time domain linearized inversion technique of Ammon *et al.* (1990). The efficacy of the modelling procedure is demonstrated using the radial RFs for station AML (Fig. 7). The computed RFs at AML are stacked to enhance the signal-to-noise ratio (red waveform in Fig. 7c) and ±1 standard deviation (SD) bounds are calculated (grey-shaded area in Figs 7b and c). These bounds are used to constrain the inverted models and to evaluate how well the observed waveforms are reproduced by inversion. This adopted technique is more sensitive to velocity contrasts rather than to the absolute magnitude of velocities and is sensitive to a starting velocity model. The starting model parameterized in terms of thin, homogeneous and horizontal layers of equal

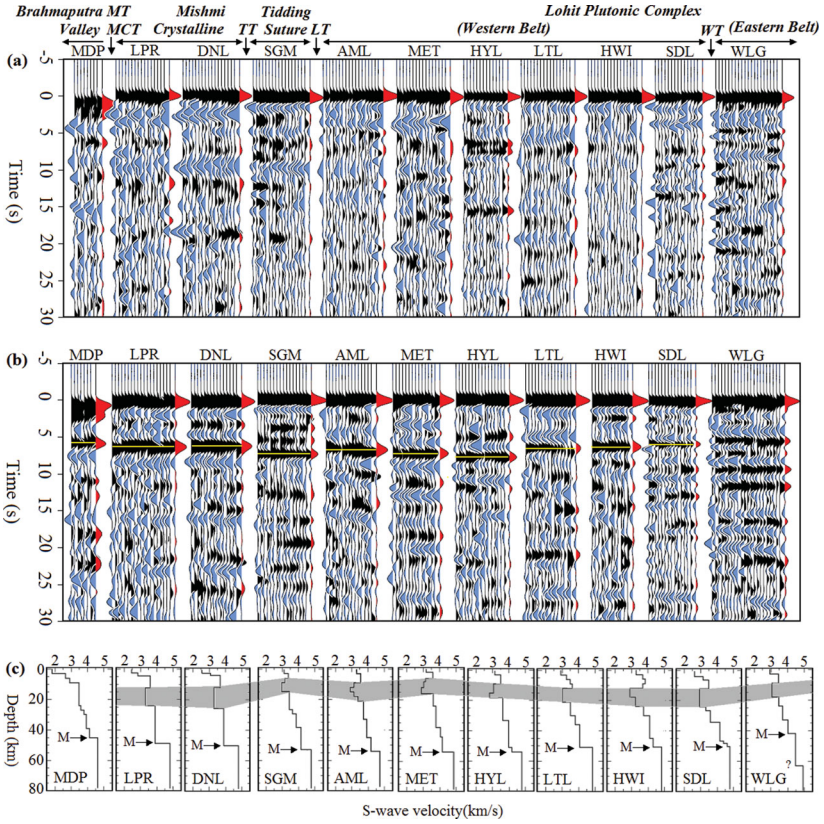

Figure 6. (a) Time section plot of radial receiver functions computed at each stations for the teleseismic earthquake waves arriving from NE direction (BAZ: 30°–80°). The red waveforms show stacked RFs at each station. The Moho converted P_ms phase is not clearly identified in the receiver functions. The major tectonic features: Mishmi Thrust (MT), Main Central Thrust (MCT), Tidding Thrust (TT), Lohit Thrust (LT) and Walong Thrust (WT) are marked in the figure. (b) Time section plot of radial RFs computed at each station combing data of earthquake waves of all directions except from NE. The plots show well defined Moho interface (marked by yellow lines). The stack receiver functions at each station are shown by red colour. Amplitude scale is same as adopted in Fig. 2 and are moveout corrected. (c) The inverted velocity models corresponding to each station obtained using SE group of RFs. The intracrustal low-velocity layer (IC-LVL) is marked by the grey shaded area.

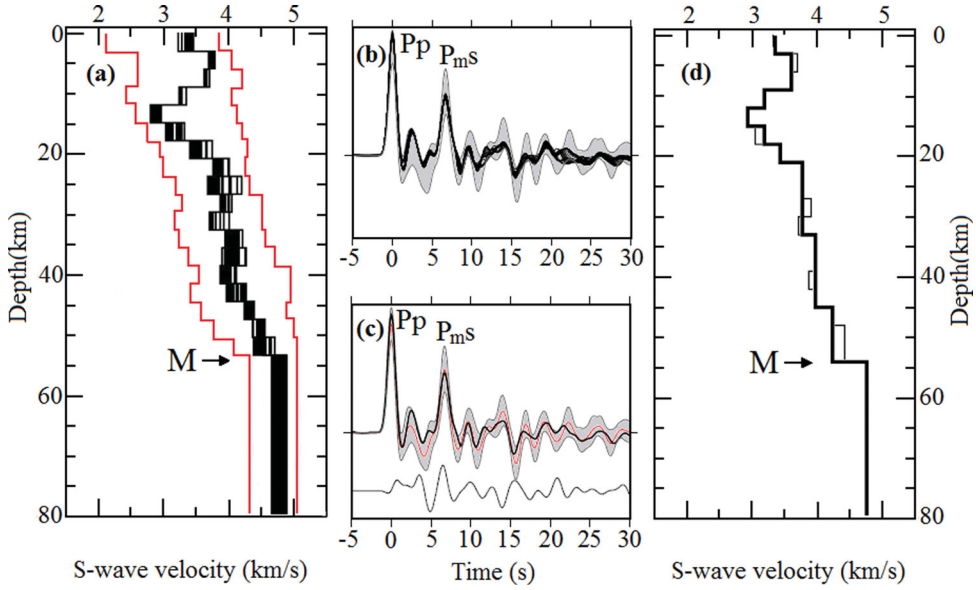

Figure 7. Inversion results of AML receiver functions. The inverted velocity models are shown on the left (a) as black solid lines where the range of starting models is indicated by red lines. The synthetic receiver functions corresponding to the range of inverted models in 'a' are shown in the middle panel (black waveforms) (b), the grey-shaded area shows ±1 SD bound of observed receiver functions. The comparison of observed (red) and synthetic (black) receiver functions is shown in panel (c) along with corresponding stacked tangential receiver function. The representative best-fitting inverted (thin black line) as well as simplified final velocity model after forward modelling (thick black line) are shown in the right panel (d).

thickness (3 km) is constructed from previous published work (Singh 1994; Mitra *et al.* 2005). This starting model is perturbed moving the interfaces up and down within a reasonable range of depth of 1 km interval based on a perturbations scheme with a cubic perturbation of 0.75 km s^{-1} (as described in Ammon *et al.* 1990). At each upgradation of the starting model, the synthetic RFs for a given velocity model is computed and the inversion seeks to minimize the difference between the observed and synthetic RF waveforms. This perturbation scheme gives a set of new starting models (Fig. 7a), allowing the exploration of a wide initial model space and reducing the dependence of the solutions on the starting model. The combination of different layer thicknesses permitted the inversion over ∼200 initial models. The stacked RF of the given station is inverted by minimizing the difference between the observed and synthetic RFs computed for range of initial models, while simultaneously constraining the model smoothness (Ammon *et al.* 1990). The models that produce synthetic RFs (black waveforms in Fig. 7b) within the ±1 SD bounds of stacked RF are plotted in one figure to classify the main features of the structure (Fig. 7a). One of the best-fitted models is selected and the main features of the structure are derived by grouping the thin layers with similar velocities into a single layer (Fig. 7d). The adjusted model is used as an initial model and inversion is repeated until we can model the dominant phases and avoid over-complexity in the resultant model. Forward modelling is used to produce the synthetic radial RF for the adjusted model and the results of the forward modelling and inversion are compared to infer the final model (Fig. 7d). It is seen that final inverted model is able to reproduce the waveform within the statistical bound of observed RF for entire time window up to 30 s, indicating that effects of scattering and anisotropy, even if present, do not bias the extraction of 1-D velocity structure in any significant manner.

The result of the inversion indicates that the upper crust at AML is characterized average *S*-wave velocity (V_s) of 3.8 km s^{-1}. There is inequitable evidence of an IC-LVL in the depth range of about 9–21 km, which is compatible with phases below ∼5 s (Figs 2–3). The velocity increases progressively in the lower crust but Moho, unambiguously marked by step jump in velocity, is detected at about 54 km depth.

4.4 *S*-wave velocity profiles

To bring out the azimuth-dependent crust-mantle structure of the indenting Indian Plate, the radial RFs for different stations are inverted separately for NE and SE groups using time domain linearized inversion method described earlier. The inverted velocity–depth profiles for both groups show near identical velocity distribution in the crustal section. However, in terms of velocity transition at Moho, some first-order differences are noted (Fig. 8). The IC-LVL with average thickness of approximately 10 km is another persistent feature of all stations of the Lohit Valley, although it varies marginally in depth, thickness as well as in terms of absolute velocity along the transect. The MDP station at Brahmaputra Valley does not show IC-LVL. The S-LVL of the order of 3 km is a characteristic of the station MDP in the Brahmaputra valley.

If we visualize Moho as the depth where there is sharp step velocity jump and where shear wave velocity in the mantle attains a value of at least 4.6 km s^{-1}, the Moho is unmistakably identified at all stations for SE back azimuth group, except two northern most stations (Fig. 6c). In contrast, for the NE back azimuth group where the P_ms phase at ∼6 s itself is diffused (Fig. 6a), the Moho is marked by gradational velocity transition over a thickness of 20 km and typical mantle velocity of > 4.6 km s^{-1} is reached at a depth of the order of ∼55 km (Fig. 8). The robustness of the inverted velocity model for the NE group showing gradational velocity change is further tested with recourse to synthetic tests. It follows from Fig. 5b that when Moho is marked by gradational velocity transition (model b), the primary phase around 6 s is broadened and highly subdued in amplitude whereas the related late multiples attain insignificant amplitude and waveform spread in time (Fig. 5b). All these are consistent with the observed patterns of SE and NE groups (Figs 6a and b). For the SE back azimuth group, variation in Moho across the Himalayan collision belt is depicted distinctly (Fig. 6c). The Moho is observed around 45 km depth beneath the Brahmaputra valley (MDP). Stations LPR and DNL located on the Mishmi crystalline have similar *S*-wave velocity profile with Moho seen around 50 ± 2 km. The velocity model at station SGM immediately east of the Tidding Suture Zone indicates ∼54-km-thick crust. The seismic stations AML, MET and HYL, nearly equally spaced with respect to the Lohit thrust on the western part of the Lohit Plutonic Complex show a uniform depth of ∼55 km to the Moho. Under the eastern part of the Lohit Plutonic Complex, the Moho shows marginal uplift with averaged depth of about 50 km. The WLG station situated further NE of the Walong thrust on the extreme fringe of the Lohit Plutonic Complex show multiple layering in the inverted velocity model. There are two equally strong velocity interfaces at 42 and 63 km depth.

5 DISCUSSION

5.1 Azimuthal variation in crustal structure

The one significant feature observed in the RFs is the absence of well-defined P_ms phase for the seismic waves arriving from northeast. By ray tracing the incident P_ms phase through the crust, we obtained the piercing points of P_ms phase for all earthquake events used for RFs analysis (Fig. 9). The piercing points for the NE group (Fig. 9, symbols filled with orange colour) scuttle a narrow area of the EHS bordering the northeastern fringe of indenting Indian plate. Because the teleseismic waves reaching different stations of the present profile are sensitive to the subsurface structure at conversion (piercing) points, consistent with the synthetic modelling (Fig. 5b), it can be surmised that due to the gradational or lack of sharp velocity jump at the Moho in this highly deformed zone, the P_ms phase is highly subdued or absent at most stations. The eastward extrusion of the Indo-China block along the Red River fault (Tapponnier *et al.* 1982; Zeitler *et al.* 2001), dominance of clockwise rotating GPS velocity vectors (Chen *et al.* 2000), evidence of rigid and thick lithospheric roots beneath the Sichuan Basin (Xu *et al.* 2007; Zhang *et al.* 2009, 2010), anomalous geothermal fluxes (Hochstein *et al.* 1998), presence of arcuate channels of extremely high electrical conductivity (Bai *et al*. 2010) individually and collectively are pointer of large-scale deformation and crustal flow around the NE corner of the EHS resulting from the oblique indentation of the Indian Plate (Gan *et al.* 2007; Sol *et al.* 2007; Xu *et al.* 2007; Zhang *et al.* 2009, 2010; Bai *et al*. 2010). It seems likely that due to these intense deformations, the step velocity jump associated with the Moho is either diminished or vanished beneath this deformed part of the EHS. At station MDP where seismic wave reach without piercing the anomalous zone (Fig. 9), the Moho converted phase can be traced in the RFs (Figs 6a and b) as well as in inverted velocity profile (Figs 8 and 6c). However, by virtue of its

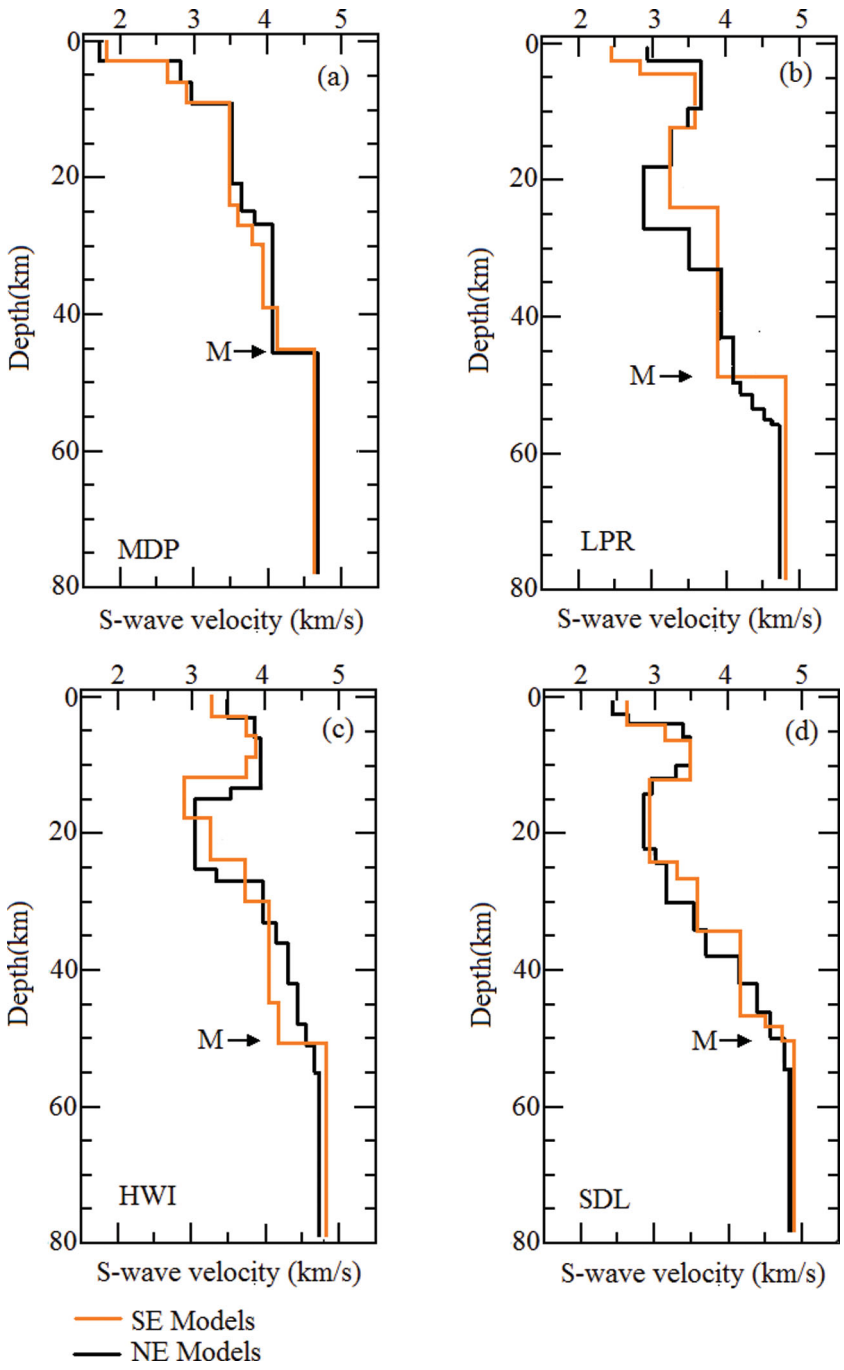

Figure 8. Comparison of shear wave velocity–depth profiles obtained by the inversion of NE and SE group separately at selected stations. The IC-LVL is a conspicuous feature of both groups. The Moho transition is marked by step velocity jump for SE group, whereas for NE group Moho is characterized by gradational velocity change.

location in Brahamputra valley has registered the thickest S-LVL of extremely low velocity (3 km thick with velocity of ∼1.5 km s^{-1}; Fig. 6c). Perhaps due to strong reverberations in this surface layer (marked by broadening of peak of direct *P* arrivals), amplitude of other converted phases are suppressed in RFs plot of Figs 6a and b.

By contrast teleseismic waves traversing the EHS deformation zone, the waves arriving at stations of the current profile from the SE azimuth pierce through the different lithotectonic blocks of the Himalaya and hence reflect the lateral variation of the subsurface structure across the Himalayan collision zone. In view of this velocity section for this azimuth alone is used in next section to constrain the structures of the Himalayan collision zone. In essence, the detection of azimuth-dependent velocity structure is facilitated by orientation of the profile vis-à-vis the location of anomalous deformed zone.

5.2 Moho geometry and extent of underthrusting

The Moho configuration from the Foredeep to Trans-Himalaya (Lohit Plutonic Complex) through the High Himalaya (Mishmi

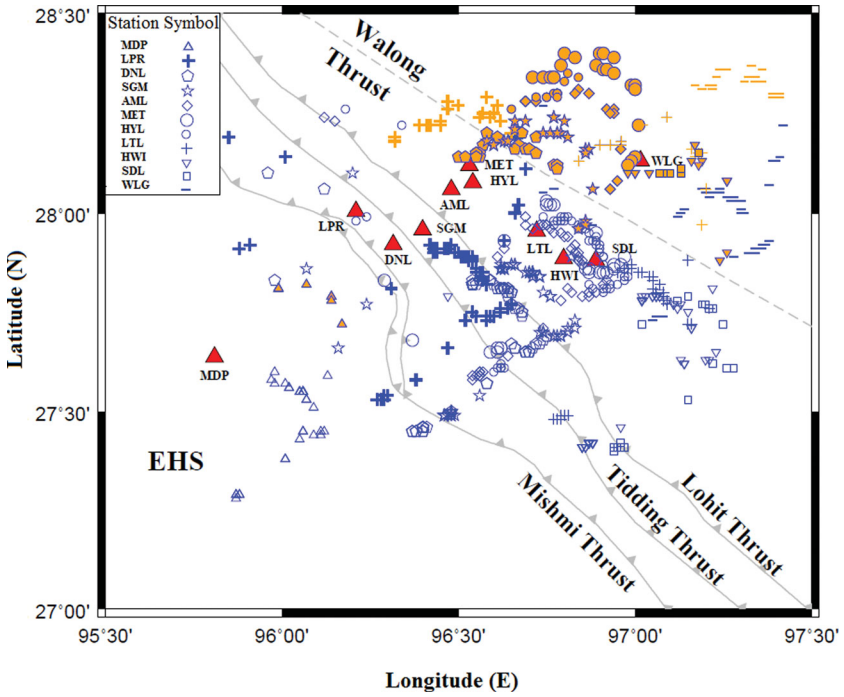

Figure 9. Location of the Moho P_ms piercing points for all the teleseismic earthquakes used for receiver function analysis. The piercing points corresponding to each recording station are shown by different symbols. The piercing points of P_ms phase for the earthquakes entering the region from NE direction (BAZ: ~30°–80°) are highlighted by orange colour.

Crystalline) can more easily be tracked in the inverted velocity models of different stations, shown in Fig. 6c. The velocity models for the SE group show progressive deepening of Moho depth from Brahmaputra valley towards northeast. The dipping structure of the Moho is consistent with the underthrusting of the Indian plate beneath the Lesser and High Himalaya. The down-going plate flattens out at the Tidding Suture Zone and continues to slide under the Asian Plate/Burma platelet (Mukhopadhyay & Dasgupta 1988; Ni *et al.* 1989). The continuity of the Moho across the Tidding Suture with no offset in this part of the collision zone is completely in agreement with the underthrusting of Moho across the ITSZ in northwest Himalaya (Rai *et al.* 2006) and in central Himalaya (Kind *et al.* 1996; Nelson *et al.* 1996). However, by contrast the Moho depth of more than 70 km in the northwest and central Himalaya, the thickened crust in the NE part of Indian Plate is only about 55 km. This may be a consequence of the slower rate of plate convergence in this section of the collision zone as against the northwest and central segment of the Himalaya. GPS measurements are clear pointer that while plate convergence across the northwest and central Himalaya are being consumed by crustal shortening at an approximate rate of 17–20 mm yr^{-1} (Bilham *et al.* 1997; Banerjee & Burgmann 2002), this rate in the northeast is only about 10–12 mm yr^{-1} (Wang *et al.* 2001; Jade *et al.* 2007). This relation between rate of convergence and crustal thickness provide strong support to the hypothesis that subsurface compensation in Himalayan collision zone is attained by the mechanism of crustal thickening (LeFort 1975; Allegre *et al.* 1984).

Fig. 10 shows an integrated picture of the Moho geometry from the Brahmaputra valley in the west to Sichuan Basin across the Lohit River valley and southeastern Tibet Plateau. The plot is constructed by adding the data to the present profile from Mikir Plateau in NE India (Mitra *et al.* 2005) to SE Tibetan Plateau (Xu *et al.* 2007), projected roughly along the latitude circle of 28°N. An unambiguous feature of the plot is the opposite dipping trend in the Moho of the two colliding Indian and SE Asian plates. The complexity of the RF images at WLG station may be pointer that the two oppositely dipping Moho converge around this station. This warrants that Indian Plate does not penetrate deep into southeastern Tibet across the EHS, unlike the northern Tibet where Indian plate thrusts right up to Bangong Suture (Tilmann *et al.* 2003; Rai *et al.* 2006), some 400 km north of the surface boundary separating the rocks of Indian and Asian Plate, that is the ITSZ.

5.3 Surface and intracrustal low-velocity layer (IC-LVL)

The IC-LVL is the most conspicuous feature of the *S*-wave velocity structure deduced for the entire length of the profile. Confined to middle crustal depths (~10–25 km), the depth to top does not always vary in unison with Moho. The presence of the IC-LVL has been widely indicated by active and passive seismic experiments in different litho-tectonic subdivisions of the Himalaya as well as the Tibet Plateau (Nelson *et al.* 1996; Li & Mooney 1998; Kind *et al.* 2002; He *et al.* 2004; Schulte-Pelkum *et al.* 2005; Xu *et al.* 2007). The two alternative candidates invoked to explain the origin of the IC-LVL include presence of partial melt resulting from shear heating (Rabinowicz & Vigneresse 2004), decompressional melting (Kind *et al.* 2002) or the metamorphic fluids released by temperature controlled dehydration reactions (Hyndman & Shearer 1989; Jones 1992). Following the successful documentation from INDEPTH experiment (Nelson *et al*. 1996; Brown *et al*. 1996; Klemperer 2006), the origin of IC-LVL accompanied by high heat flow (Hochstein *et al.* 1998) and extremely low-resistivity layer with overall conductance of several thousand Siemens (Unsworth *et al.* 2005; Arora *et al.* 2007; Bai *et al.* 2010) is attributed to partial melting. In comparison, the IC-LVL characterized by relatively lower order velocity reduction

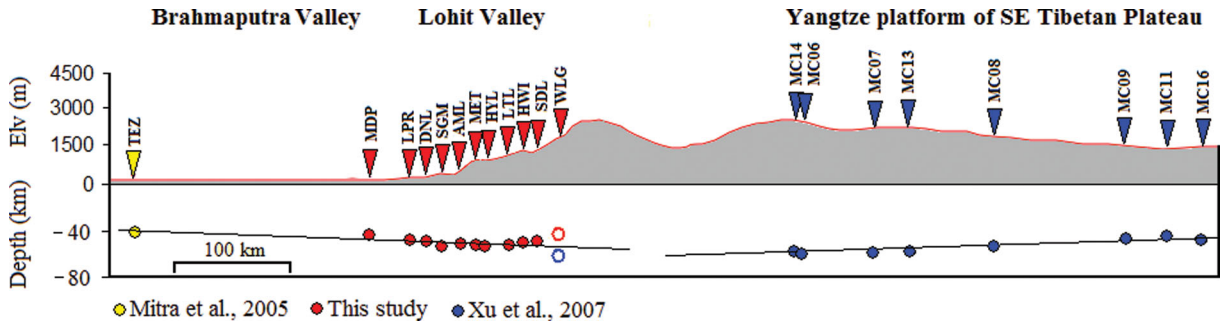

Figure 10. The upper part of the figure shows change in elevation; the lower part displays the variation of Moho geometry from Mikir plateau, NE India (Mitra *et al.* 2005) to Yangtze platform, SE Tibetan Plateau (Xu *et al.* 2007) across the Lohit Valley. Filled circles with different colours show opposite dipping Indian and SE Asia plates that appear to converge near station Walong (WLG). The 42 and 63 km discontinuities observed at WLG station are indicated by red and blue open circles, respectively.

and moderate conductance (<3000 S), the trapped fluids released by chain of dehydration reactions are considered potential candidate (Jones 1992; Arora 2003; Kumar *et al*. 2009; Schulte-Pelkum *et al.* 2005). More recently Xu *et al.* (2007) reviewing sources for crustal velocity reductions have deduced that lower shear wave velocity of ∼3.0–3.2 km s^{-1} in the IC-LVL (∼10–30 km) or shear wave velocity reduction of 12–19 per cent relative to the velocity of upper crust are indicative of partial melting with melt fraction of 4 per cent. Adopting this as a guideline, it can be surmised that both partial melt and hydrated-fluid mechanism are operative to produce IC-LVL across the present profile. At stations north of the Tidding Suture, shear wave velocity reduction in the mapped IC-LVL are higher than the threshold value observed by Xu *et al.* (2007). Here, the velocity reduction at individual station range between 14 and 21 per cent of the upper crustal velocity, partial melt is most likely cause for the IC-LVL beneath the Lohit Plutonic Complex, north of the Tidding Suture. At stations south of the Tidding Suture, velocity reduction is typically of the order of 10 per cent and, thus, suggests that fluids generated by dehydration reactions or expelled from the compaction of sediments underthrusted with the down-going Indian plate may be the primary source for the IC-LVL in this profile. The sharp reduction in the shear wave velocity at midcrustal depths from beneath the High Himalaya to the Trans-Himalayan blocks across the ITSZ is also evident from the recent results of Caldwell *et al.* (2009) from the northwest Himalaya. Well developed transition in low resistivity across the ITSZ, coinciding with velocity change was earlier reported by Arora *et al*. (2007).

6 CONCLUSIONS

Receiver function analysis of teleseismic earthquakes recorded at 11 stations along the Lohit River Valley profile cutting across the Tidding Suture, marking India-Asia collision zone at the eastern end of the Himalayan arc, show an azimuthally varying crustal structure in the region. The majority of RFs computed for earthquakes entering the study region from the northeast back azimuths (∼30°–80°) do not show Moho converted P_ms phase. The velocity inversion and synthetic RF for a given velocity model suggest that the step velocity jump at the Moho is absent beneath the localized zone scuttled by piercing rays. It is surmised that due to large-scale deformation resulting in response to the compression forces generated by indenting Indian Plate, the crust–mantle transition in the region immediately bordering the EHS is marked by gradational velocity change.

The teleseismic waves arriving from other back azimuths sample, different litho-tectonic blocks of the Himalaya collision zone and time section plots of radial RFs reveal well-defined P_ms phase at all stations. The *S*-wave velocity profile obtained by the inversion of RFs for of this azimuth group help to trace the geometry of Moho across the NE corner of the India-Asia collision belt, which is found to be a replica of that observed across the northwest and central Himalaya. The observed NE dipping structure of Moho from the Himalayan foredeep (Brahmaputra valley) to the Trans-Himalayan region (Lohit Plutonic Complex) with no offset across the collision zone (Tidding Suture) is consistent with underthrusting of the Indian Plate beyond the surface collision boundary. However, in this section of the Himalaya the average thickness of crust is ∼55 km, which is much less compared to that observed in the central and northwest Himalaya (∼70 km). In agreement with GPS measurements, this is attributed to the slower rate of convergence in the northeast. The synthesized picture of the Moho geometry obtained by combining data from Shillong-Mikir Plateau to Yangtze Platform (SE Tibetan Plateau) reveal opposite dip. The trend of the dipping Moho can be construed to infer that two colliding plates converge immediately east of the Walong Thrsut.

Further *S*-wave velocity inversions have given evidence on the intracrustal low-velocity zones. The magnitude of velocity reductions favour both partial melt as well as fluids generated by dehydration reactions may be the source mechanisms for velocity reductions in different parts of the profile. The correlation with on-going magnetotelluric measurements would also be helpful to ascertain cause of low-velocity zones.

ACKNOWLEDGMENTS

This study is part of the coordinated program on 'Himprobe Northeast' under the umbrella of 'Deep Continental Studies in India', sponsored by the Department of Science & Technology (DST), Government of India. The financial support and encouragement received from the DST and members of the project monitoring committee are acknowledged with thanks. The encouragement and facilities provided by the host Institutions is recorded with gratitude. One of us (BRA) thanks CSIR, India for Emeritus Scientist Fellowship. The support provided by Mr. V. Sriram and Dr D. K. Yadav in field operations and initial data preparations is deeply appreciated. Many fruitful discussions with Drs. V.C. Thakur and A.K. Dubey helped to understand fine aspects of the geology and tectonics of the study region, whereas exchange of notes with Drs. Ravi Kumar, Arun Singh, S. Mitra and D. Saikia helped to understand the

interpretation intricacies of RFs. The critical comments from two anonymous reviewers helped to improve the original version of the manuscript are gratefully acknowledged.

REFERENCES

Allegre, C.J. *et al*., 1984. Structure and evolution of the Himalaya—Tibet orogenic belt, *Nature,* **307,** 17–22.

Arora, B.R., 2003. Seismotectonics of the Frontal Himalaya through the electrical conductivity imaging, in *Seismotectonics in Convergent Plate Boundary,* pp. 261–272, eds. Fujinawa, N. & Yoshida, A., Terra Publications, Tokyo.

Arora, B.R., Unsworth, M.J. & Rawat, G., 2007. Deep resistivity structure of the northwest Indian Himalaya and its tectonic implications, *Geophys. Res. Lett*., **34,** L04307, doi:10.1029/2006GL029165.

Ammon, J.C., Randal, G.E. & Zandt, G., 1990. On the nonuniqueness of receiver function inversions, *J. geophys. Res.,* **95,** 15 303–15 318.

Bai, D. *et al*., 2010. Crustal deformation of the eastern Tibetan plateau revealed by magnetotelluric imaging, *Nature Geosci*., **3,** 358–362, doi:10.1038/NGEO830.

Banerjee, P. & Burgmann, R., 2002. Convergence across the northwest Himalaya from the GPS measurement, *Geophys. Res. Lett.,* **29,** 1652, doi:10.1029/2002GL015184.

Beaumont, C., Jamieson, R.A., Nguyen, M.H. & Lee, B., 2001. Himalayan tectonics explained by extrusion of a low-viscosity crustal channel coupled to focused surface denudation, *Nature,* **414,** 738–742. doi:10.1038/414738a.

Bird, P., 1978. Initiation of intracontinental subduction in the Himalaya, *J. geophys. Res.,* **83,** 4975–4987.

Bilham, R., Larson, K., Freymueller, J., Project Idylhim members, 1997. GPS measurements of present-day convergence across the Nepal Himalaya, *Nature,* **386**(6620), 61–64.

Brown, L.D. *et al*., 1996. Bright spots, structure, and magmatism in Southern Tibet from INDEPTH seismic reflection profiling, *Science,* **274,** 1688–1690.

Chen, Z. *et al*., 2000. Global Positioning System measurements from eastern Tibet and their implications for India/Eurasia intracontinental deformation, *J. geophys. Res.,* **105**(B7), 16 215–16 227.

Caldwell, W.B., Klemperer, S.L., Rai, S.S. & Lawrence, J.F., 2009. Partial-melt in the upper-middle crust of the northwest Himalaya revealed by Rayleigh wave dispersion, *Tectonophysics,* **477,** 58–65.

Cassidy, J.F., 1992. Numerical experiments in broadband receiver function analysis, *Bull. seism. Soc. Am.,* **82,** 1453–1474.

Gan, W., Zhang P., Shen Z.-K., Niu Z., Wang, M., Wan, Y., Zhou, D. & Cheng, J., 2007. Present-day crustal motion within the Tibetan Plateau inferred from GPS measurements, *J. geophys. Res.,* **112,** B08416, doi:10.1029/2005JB004120.

Gansser, A., 1964. *Geology of the Himalayas,* Wiley, London, 289 pp.

Gururajan, N.S. & Choudhuri, B.K., 2003. Geology and tectonic history of the Lohit Valley, Eastern Arunachal Pradesh, *J. Asian Earth Sci.,* **21,** 731–741.

He, Z.Q., Ye, T.L. & Su, W., 2004. S-wave velocity structure of the middle and upper crust in the Yunnan region, Chinese, *J. Geophys.,* **47** (5), 838–844 (in Chinese).

Hochstein, M.P. & Regenauer-Lieb, K., 1998. Heat generation associated with collision of two plates: the Himalayan geothermal belt, *J. Volc. Geotherm. Res.,* **83,** 75–92.

Holt, W.E., Ni, J.F., Wallace, T.C. & Haines, A.J., 1991. The active tectonics of the Eastern Himalayan Syntaxis and surrounding regions, *J. geophys. Res.,* **96**(B9), 14 595–14 632.

Hyndmann, R.D. & Shearer, P.M., 1989. Water in the lower continental crust: modelling magnetotelluric and seismic reflection results, *Geophys. J. Int.,* **98,** 343–365.

Jade, S. *et al*., 2007. Estimates of interseismic deformation in Northeast India from GPS measurements, *Earth planet. Sci. Lett.,* **263,** 221–234.

Jones, A.G., 1992. Electrical properties of the lower continental crust, continental lower crust, in *Developments in Geotectonics,* pp. 81–143, eds. Fountain, D.M., Arculus, R. & Kay, R.W., Elsevier, Amsterdam.

Kennett, B.L., 1983. *Seismic Wave Propagation in Stratified Media,* Cambridge University Press, Cambridge, 352 pp.

Klemperer, R.L., 2006. Crustal flow in Tibet: geophysical evidence for the physical state of the Tibetan lithosphere and inferred patterns of active flow, *Geol. Soc. Lond. Spec. Pub.,* **268,** 39–70, doi:10.1144/GSL.SP.2006.268.01.04.

Kosarev, G., Kind, R., Sobolev, S.V., Yuan, X., Hanka, W. & Oreshin, S., 1999. Seismic evidence for a detached Indian lithosphere mantle beneath Tibet, *Science,* **283,** 1306–1309.

Kind, R., Kosarev, G. & Peterson, N. V., 1995. Receiver functions at the stations of the German Regional Seismic Network (GRSN), *Geophys. J. Int.,* **121,** 191–202.

Kind, R. & Project INDEPTH team, 1996. Evidence from earthquake data for a partially molten crustal layer in southern Tibet, *Science,* **274,** 1692–1694.

Kind, R. *et al*., 2002. Seismic images of crust and upper mantle beneath Tibet: evidence for Eurasian plate subduction, *Science,* **298,** 1219–1221.

Kumar, M.R., Raju, P.S., Devi, E.U., Saul, J. & Ramesh, D.S., 2004. Crustal structure variations in northeast India from converted phases, *Geophys. Res. Lett.,* **31,** L17605, doi:10.1029/2004GL020576.

Kumar, P., Yuan, X., Kind, R. & Ni, J., 2006. Imaging the colliding Indian and Asian lithospheric plates beneath Tibet, *J. geophys. Res.,* **111,** doi:10.1029/2005JB003930.

Kumar, N., Sharma, J., Arora, B.R. & Mukhopadhyay, S., 2009. Seismotectonic model of the Kangra-Chamba sector of Northwest Himalaya: constraints from joint hypocenter determination and focal mechanism, *Bull. seism. Soc. Am.,* **99,** 95–109.

Langston, C.A., 1979. Structure under Mount Rainer, Washington, inferred from teleseismic body waves, *J. geophys. Res.,* **84,** 4749–4762.

LeFort, P., 1975. Himalayas—collided range—present knowledge of continental arc, *Am. J. Sci.,* **A275,** 1–44.

Ligorria, J.P. & Ammon, C.J., 1999. Iterative deconvolution and receiver-function estimation, *Bull. seism. Soc. Am.,* **89,** 1395–1400.

Li, C., van der Hilst, D., Meltzer, A.S. & Engdahl, E.R., 2008. Subduction of the Indian lithosphere beneath the Tibetan Plateau and Burma, *Earth planet. Sci. Lett.,* **274,** 157–168, doi:10.1016/j.epsl.2008.07.016.

Li, S. & Mooney, W.D., 1998. Crustal structure of China from deep seismic sounding profile, *Tectonophysics,* **288,** 105–113.

Mattauer, M., 1986. Intracontinental subduction, crust–mantle decollement and crustal stacking wedge in the Himalayas and other collisional belts, *Geol. Lond. Spec. Pub.,* **19,** 37–50, doi:10.1144/GSL.SP.1986.019.01.02.

Mitra, S., Priestley, K., Bhattacharyya, A.K., & Gaur, V.K., 2005. Crustal structure and earthquake focal depths beneath northeastern India and southern Tibet, *Geophys. J. Int.,* **160,** 227–248.

Molnar, P., 1988. A review of geophysical constraints on the deep structure of the Tibetan Plateau, the Himalaya and the Karakoram, and their tectonic implications, *Philos. Trans. R. Soc. Lond.,* A **326,** 33–88.

Molnar, P. & Tapponnier, P., 1975. Cenozoic tectonics of Asia: effects of a continental collision, *Science,* **189,** 419–426.

Mukhopadhyay, M. & Dasgupta, S., 1988. Deep structure and tectonics of the Burmese arc: constraints from earthquake and gravity data, *Tectonophysics,* **149,** 299–322.

Nabelek, J. *et al*., 2009. Underplating in the Himalaya-Tibet collision zone revealed by the Hi-CLIMB experiment, *Science,* **325,** 1371–1374.

Nelson, K.D. *et al*., 1996. Partially molten middle crust beneath southern Tibet: synthesis of Project INDEPTH results, *Science,* **274,** 1684–1688.

Nolet, G. & Dahlen, F., 2000. Wave front healing and the evolution of seismic delay times, *J. Geophys. Res.,* **105,** 19 043–19 053.

Ni, J. & Barazangi, M., 1984. Seismotectonics of the Himalayan collision zone: geometry of the underthrusting Indian plate beneath the Himalaya, *J. geophys. Res.,* **89,** 1147–1163.

Ni, J.F., Guzman-Speziale, M., Bevis, M., Holt W.E., Wallace, T.C. & Seager, W.R., 1989. Accretionary tectonics of Burma and the three-dimensional geometry of the Burma subduction zone, *Geology,* **17,** 68–71.

Rai, S.S., Priestley, K., Gaur, V.K., Mitra, S., Singh, M.P. & Searle M., 2006. Configuration of the Indian Moho beneath the NW Himalaya and Ladakh, *Geophys. Res. Lett.,* **33,** L15308, doi:10.1029/2006GL026076.

Rabinowicz, M. & Vigneresse, J.L. 2004. Melt segregation under compaction and shear channelling: application to granitic magma segregation in a continental crust, *J. geophys. Res.,* **B109,** doi:10.1029/2002JB002372.

Replumaz, A. & Tapponnier, P., 2003, Reconstruction of the deformed collision zone Between India and Asia by backward motion of lithospheric blocks, *J. geophys. Res.,* **108,** 2285, doi:10.1029/2001JB000661.

Savage, M.K., 1998. Lower crust anisotropy or dipping boundaries? Effect on receiver function and a case study in New Zealand, *J. geophys. Res.* **103**(B7), 15 069–15 087.

Savage, M.K., 1999. Seismic anisotropy and mantle deformation: what have we learned from shear wave splitting? *Rev. Geophys.,* **37,** 65–106.

Schulte-Pelkum, V., Monsalve G., Sheehan A., Pandey, M.R., Sapkota, S., Bilham, R. & Wu F., 2005. Imaging the Indian subcontinent beneath the Himalaya, *Nature,* **435,** 1222–1225, doi:10.1038/nature03678.

Singh, D.D., 1994. Shear wave velocity structure over the eastern Indian subcontinent, *Tectonophysics,* **230,** 127–134.

Sol, S. *et al*., 2007. Geodynamics of the southeastern Tibetan Plateau from seismic anisotropy and geodesy, *Geology,* **35,** 563–566, doi:10.1130/G23408A.1.

Tapponnier, P., Peltzer, G., Le Dain, A.Y., Armijo, R. & Cobbold, P., 1982. Propagating extrusion tectonics in Asia: new insights from simple experiments with plasticine, *Geology,* **10,** 611–616.

Tapponnier, P. *et al*., 1990. The Ailao Shan/Red River metamorphic belt: tertiary left-lateral shear between Indochina and South China, *Nature,* **343,** 431–437.

Thakur, V.C. & Jain, A.K., 1975. Some observation on deformation, metamorphism and tectonic significance of the rocks of some parts of Mishmi hills, Lohit district (NEFA), Arunachal Pradesh. *Him. Geol.,* **5,** 339–364.

Tilmann, F. & Ni, J., INDEPTH III Seismic Team, 2003. Seismic imaging of the downwelling Indian lithosphere beneath central Tibet, *Science,* **300,** 1424–1427.

Unsworth, M.J., Jones, A.G., Wei, W., Marquis, G., Gokarn, S.G., Spratt, J.E. & INDEPTH-MT team, 2005. Crustal rheology of the Himalaya and southern Tibet inferred from magnetotelluric data, *Nature,* **438,** 78–81.

van der Meijde, M., van der Suzan, L. & Domenico, G., 2003. Crustal structure beneath broad-band seismic stations in the Mediterranean region, *Geophys. J. Int.,* **152,** 729–739.

Vinnik, L.P., 1977. Detection of waves converted from P to SV in the mantle, *Phys. Earth planet. Inter.,* **15,** 39–45.

Wang, Q. *et al*., 2001. Present-day crustal deformation in China constrained by global positioning system measurements, *Science,* **294,** 574–577.

Xu, L., Rondenay, S. & van der Hilst, R.D., 2007. Structure of the crust beneath the southeastern Tibetan Plateau from teleseismic receiver functions, *Phys. Earth. Planet Int.,* **165,** 176–193, doi:10.1016/j.pepi.2007.09.002.

Zeitler, P.K. *et al*., 2001. Erosion, Himalayan geodynamics, and the geomorphology of metamorphism, *GSA Today,* **11,** 4–9.

Zhang, Z.J., Wang, Y.H., Chen, Y., Tian, X.B., Houseman, G., Wang, E. & Teng, J.W., 2009. Crustal structure across Longmenshan fault belt from passive source seismic profiling, *Geophys. Res. Lett.,* **36,** L17310, doi:10.1029/2009GL039580.

Zhang Z., Yuan, X., Chen, Y., Tian, X., Kind, R., Li, X. & Teng, J., 2010. Seismic signature of the collision between the east Tibetan escape flow and the Sichuan Basin, *Phys. Earth planet. Inter.,* **292,** 254–264, doi:10.1016/j.epsl.2010.01.046.